Numerical simulation of quasibrittle fracture in concrete

Mario M. Attard *, Francis Tin-Loi

School of Civil and Environmental Engineering, University of New South Wales, Sydney NSW 2052, Australia

Abstract

A triangular unit, constructed from constant strain triangles with nodes along its sides and not at the vertex, is developed for the simulation of fracture in quasibrittle materials. Fracture is modelled through a constitutive softening–fracture law at the interface nodes, with the material within the triangular unit remaining linear elastic. The inelastic displacement at an interface node represents the crack opening, which is related to the conjugate inter-nodal force by the appropriate softening relationship. The path-dependent softening behaviour is solved in nonholonomic rate form within a quasiprescribed displacement formulation. At each event in the loading history, all equilibrium solutions for the prescribed mesh can be established and the critical equilibrium path with the minimum increment of external work adopted. The crack profile or trajectory is restricted in that it can only follow the interface boundaries of the defined mesh. No remeshing is carried out. Solutions to the nonholonomic rate formulation are obtained using a mathematical programming procedure based on the solution of an LCP. Several examples are given and compared, where possible, with published results. The advantage of this formulation is that branching and interacting cracks can be tracked subject to the limitations of the prescribed mesh.
© 2004 Elsevier Ltd. All rights reserved.

1. Introduction

Over the last decade there has been intense research interest in the modelling of fracture in quasibrittle materials. Most of the investigations have been limited to mode I failure. The various methods proposed can be broken into two main classes: the discrete crack methods and those based on a continuum model with smeared cracking. The formidable difficulties in providing a numerical simulation of the fracturing process within quasibrittle materials lie with the fact that the fracturing zone consists of discontinuous cracks and shear bands where damage is localized. The localization is associated with softening of the load carrying capacity. Since the crack opening is discontinuous, it cannot easily be handled by continuum models.

Generalised continuum theories such as Cosserat continuum and rate-dependent continuum have been developed (Li and Cescotto [1]). De Borst [2] gives an overview of continuum damage-based approaches

---

* Corresponding author. Tel.: +61-2-9385-5075; fax: +61-2-9385-6139.
E-mail address: m.attard@unsw.edu.au (M.M. Attard).

used to study fracture in quasibrittle materials. He shows that the smeared-crack models can be cast into a damage format and can be conceived as a special case of anisotropic damage models.

Softening and strain localization can give rise to computational problems because of the possibility of multiple solutions to the equilibrium path (e.g., Bolzon et al. [3]). This is evident when there are two or more locations which simultaneously reach their inelastic failure/yield point and have the option of either softening or elastically unloading. The two notched tensile problem was shown to have multiple paths associated with whether the loading platens rotate or are held fixed.

The discrete crack methods take account of cracking by defining a boundary to the finite element (or boundary element) mesh along the crack path, concentrating inelasticity along this boundary and allowing the crack to open between the finite elements that remain linearly elastic. Consideration of the fracture process zone ahead of the crack tip is also essential and can be incorporated using the fictitious crack model of Hillerborg et al. [4]. The crack tip is extended over a fictitious length over which the opening normal to the crack is related to the normal traction by a softening law having an enclosed area equal to the fracture energy. The process zone is limited to the fictitious crack length. The fictitious crack or cohesive zone model has several limitations discussed by Elices et al. [5] and Bazant [6].

Bolzon et al. [3,7] use a novel approach for a predefined crack profile where the discrete crack model is formulated as a linear complementarity problem (LCP) and solutions are sought using mathematical programming algorithms. One of the advantages of this approach is that all possible equilibrium paths subject to the crack following the predefined crack profile can theoretically be followed. A disadvantage is that there is generally no guarantee that all solutions can be obtained in finite computation time and importantly, the crack profile has to be predefined.

The discrete crack methods often require remeshing, with the crack path determined by the trajectory of the principal tensile stress in mode I, unless the crack profile is known a priori, as in a well-conducted three point bending test. A challenge to the discrete-crack approach is the computationally demanding adaptive remeshing required to correctly predict crack branching, crack bridging and the interaction between developing cracks. Recently, Carol et al. [8] presented an interface element approach for modelling normal/shear cracking in quasibrittle materials that can be used either in the context of a discrete crack analysis or of a smeared crack analysis.

Lattice type models, such as those developed by Van Mier et al. [9] and Schlangen [10], have also been proposed in an attempt to predict the response of concrete at the meso-level. A concrete continuum is modelled using a triangular lattice composed of beam elements connected at nodes. The heterogeneous material properties of concrete are incorporated by distinguishing between regions representing the aggregate, mortar and aggregate–mortar interface and selecting a mesh with randomly generated beam orientations. To simulate the fracture process and growth of cracking, a step-by-step linear elastic analysis is carried out. Subject to a fracture law, ''single'' beam elements are removed one at a time, as appropriate, and the analysis continued. This approach does not permit any bifurcation to the equilibrium path as there is a unique solution at each step. Some of the major drawbacks of the lattice models are: if a crack closes there is no prevention of overlap, there is no reconnection of elements in contact and there is no account taken of friction when crack surfaces in contact move across one another. Because of these shortcomings, the present lattice models have limited success in simulating concrete under compressive loading. Van Mier's lattice approach does provide simulations which predict reasonable crack paths and phenomenon such as crack face bridging and branching.

Models which represent concrete as an assemblage of particles have also been proposed in Zubelewicz and Bazant [11], Bazant et al. [12] and Beranek and Hobbelman [13]. These particle type approaches attempt to more closely model the structure of concrete and recognize the heterogeneous nature of concrete. Usually, particles are assumed to be rigid or linear elastic and the fracture/softening effects are concentrated in the interface contact zone. A particle representation only approximates a continuum depending on the density of voids. The particle and lattice models can both be classified as ''interface'' type models.
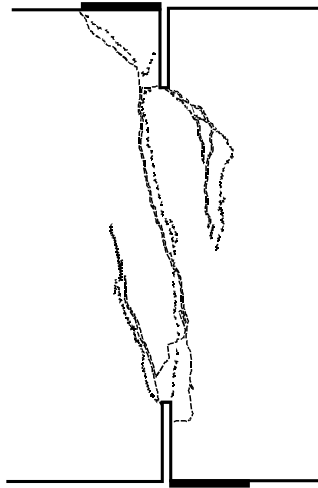
Fig. 1. Experimental crack pattern for the DEN test with fixed supports showing several interacting and branching cracks (Schlangen [22]).

The discrete element representation proposed by Attard and Tin-Loi [14] is also a particle/interface type model. The present paper discusses and extends the capabilities of this initial attempt and presents further results. The formulation is based on a linear complementarity formulation as in Bolzon et al. [3,7] and uses a mathematical programming algorithm to obtain solutions to a nonholonomic rate formulation. A softening single branch constitutive law is used. When multiple equilibrium solutions are detected, the solution with the minimum incremental external work is chosen as the critical solution. The advantages of this formulation are that, as with the discrete crack models, there is no length scale required. The challenge for the simulation of fracture is to incorporate the heterogeneous nature of concrete and devise strategies to track interacting and/or branching cracks as for example in DEN test with fixed supports (see Fig. 1). The proposed formulation attempts to do this without remeshing.

2. Discrete triangular unit

The basic unit in the formulation is a triangle formed by assembling nine constant strain triangles and condensing out the freedoms at the vertices (Fig. 2a). There are two nodes on each of the three sides/interfaces of the triangle unit. The position of the interface nodes is set at $L_i/2n$ from the vertices, where L_i is the interface length (length of the side of the triangular unit) and n is a chosen number (Fig. 2a). In this paper "n" has been set at a value of 10. This ensures that the elastic displacement predictions of the model closely match those from a continuum formulation.

The material within the triangular unit remains linear elastic if the constitutive relationship for the interface forces is of the softening type. Generalized interface displacements are defined and correspond to the outward normal and tangential (anticlockwise defined as positive) displacements at the interface nodes. The conjugate generalized forces are the outward normal and shear forces at the interface nodes (Fig. 2a). The term "generalized" is used to indicate that the system of interface forces and displacements carry out the same work as the system of applied forces and conjugate displacements.

For the assembled single triangular unit, the relationship between the forces at the interface nodes in the directions of a global rectangular axis system and the generalized interface forces is given by

$$\mathbf{A}_u \mathbf{Q}_u = \mathbf{F}_u \tag{1}$$

(a) Discrete Triangular Unit

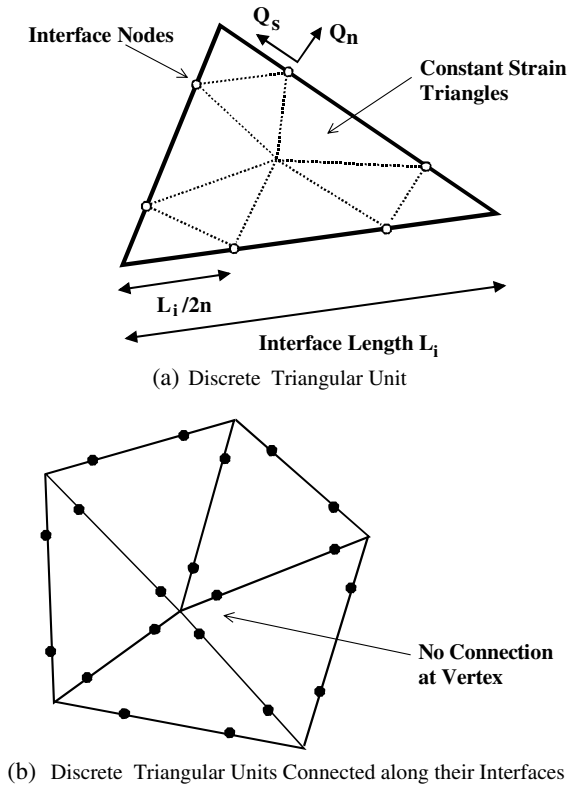(b) Discrete Triangular Units Connected along their Interfaces

Fig. 2. Discrete triangular units.

where $\mathbf{A}_u$ is an equilibrium matrix, $\mathbf{Q}_u$ a vector of generalized interface forces and $\mathbf{F}_u$ a vector of nodal forces. The matrix $\mathbf{A}_u$ is a block diagonal matrix of the form $\mathbf{A}_u = \mathrm{diag}[\mathbf{R}_1, \mathbf{R}_1, \mathbf{R}_2, \mathbf{R}_2, \mathbf{R}_3, \mathbf{R}_3]$ with the $\mathbf{R}_i$ matrices representing the rotation matrices required to transform the generalized interface forces to the global axis system. From contragradience, the relationship between the displacements at the interface nodes and the generalized interface displacements is therefore

$$\mathbf{A}_u^{\mathbf{T}}\mathbf{u}_u = \mathbf{q}_u \tag{2}$$

with $\mathbf{u}_u$ being the vector of nodal displacements and $\mathbf{q}_u$ the vector of generalized interface displacements. The element elastic stiffness matrix $\mathbf{K}_u$, assuming small displacements, can be assembled from conventional constant strain triangles with the triangular unit vertex freedoms condensed. Hence, for the triangular unit, we have

$$\mathbf{K}_u\mathbf{u}_u = \mathbf{F}_u \tag{3}$$

Since the equilibrium matrix in (1) is invertible, we can write

$$\mathbf{S}_u\mathbf{q}_u = \mathbf{Q}_u \tag{4}$$

where

$$\mathbf{A}_u^{-1}\mathbf{K}_u(\mathbf{A}_u^{\mathbf{T}})^{-1} = \mathbf{S}_u \tag{5}$$

and $\mathbf{S}_u$ is the stiffness matrix for the single triangular unit relating the generalized interface actions.

A body is modelled by using a discrete mesh generated using an algorithm such as Delaunay triangulation. The triangular units are, however, only connected at the interface nodes. The generalized interface forces across any connected interface must therefore be equal in magnitude but opposite in sign. The model, it should be noted, only approximates a continuum since the vertices are not connected (Fig. 2b) providing, moreover, a good idealization of voids and contact surfaces that would exist. Cracking is thus represented by the opening or closing across the interfaces of the triangular units.

For the complete structure, the vectors and the matrices defined above are collected to form the traditional supervectors **F**, **Q**, **q** and **u**; **A** is assembled on a structural level and **S** is an assembled block-diagonal matrix, with the subscript *u* dropped. The structure stiffness matrix **K**, is thus given by

$$\mathbf{K} = \mathbf{A}\mathbf{S}\mathbf{A}^{\mathbf{T}}$$ (6)

3. Inelastic failure surface and constitutive law

The inelastic failure surface can be approximated by a piecewise linear representation of "yield" surfaces, as in classical plasticity (Maier, [15]). At the level of the interface nodes, the inelastic failure surface is a function of the normal and shear interface forces. Fig. 3 depicts a typical interface inelastic failure surface. Clearly, it follows the classical Mohr–Coulomb type law with a tension cut-off. It is important to note that the inelastic failure surface adopted herein involves interface generalized stresses (forces), as opposed to actual stresses used in conventional continuum models.

In the Hillerborg fictitious crack model, mode I fracture is initiated along a crack path defined by the principal tensile stress. The process zone is assumed to lie along a line just ahead of the critical, about to fully develop crack. As pointed out in Bazant [12], however, the crack path under pure tension within a heterogeneous material such as concrete, is usually jagged and follows the weak interface zones around the aggregate particles. The damaged area ahead of the crack is localized within a band region. Mixed mode inelastic failure surfaces have been proposed in the literature, see e.g., Carol et al. [8]. Beranek and Hobbleman [13] modelled concrete as an assemblage of equal spheres and were able to determine a inelastic failure criterion for the contact layer for the spheres in terms of the contact normal and shear stresses. The inelastic failure criterion was a hyperbolic function. The strength in tension was determined as the same in shear, which they noted, is just as Coulomb had suggested.
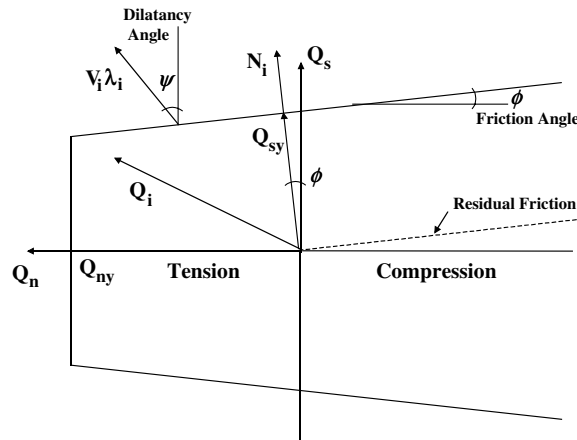

Fig. 3. Interface inelastic failure surface.

In the present particle representation, the orientations of the interfaces do not usually line up normal to the principal tensile stress directions unless modelled to do so. Hence, most interfaces will be subject to a combination of tension and shear.

For the nodal interface inelastic failure surface shown in Fig. 3, $\boldsymbol{\lambda_i}$ is the interface multiplier vector (analogous to plastic multipliers used in plasticity) given by

$$\boldsymbol{\lambda_i} = \begin{bmatrix} \lambda_n \\ \lambda_{s1} \\ \lambda_{s2} \end{bmatrix} \tag{7}$$

where λ_n is the multiplier associated with the tension cut-off of the interface inelastic failure surface and, λ_{s1} and λ_{s2} are the multiplier associated with the Mohr–Coulomb portions of interface inelastic failure surface; Q_i is the resultant force vector at the interface node, Q_{ny} is the inelastic failure normal force and Q_{sy} is the shear inelastic failure force. The interface normality matrix $\mathbf{N_i}$ and the dilatancy matrix $\mathbf{V_i}$ are given, respectively, by

$$\mathbf{N_i} = \begin{bmatrix} 0 & \cos\phi & -\cos\phi \\ 1 & \sin\phi & \sin\phi \end{bmatrix} \tag{8}$$

$$\mathbf{V_i} = \begin{bmatrix} 0 & \cos\psi & -\cos\psi \\ 1 & \sin\psi & \sin\psi \end{bmatrix} \tag{9}$$

The angle ϕ is the friction angle and ψ is the dilatancy angle (assumed to be constant in the present work). Clearly, the flow rule is associated when inelastic failure is initiated by tension and nonassociated when initiated by shear with different friction and dilatancy angles. The normal inelastic failure force Q_{ny} is estimated from the product of the material tensile strength stress f_t obtained from a pure tension test, with half the interface length L_i and the interface thickness t_i. That is,

$$Q_{ny} = \frac{f_t L_i t_i}{2} \tag{10}$$

This is an average measure of the inelastic failure capacity since the traction along the interface will not normally be uniform. Cracking, initiated by inelastic failure of the normal interface force, produces only an inelastic displacement normal to the interface. Likewise, the shear inelastic failure force Q_{sy} is the product of the shear strength stress, half the interface length and the interface thickness. The failure forces are conveniently collected in the initial inelastic failure vector $\mathbf{r_i}$ given by

$$\mathbf{r_i} = \begin{bmatrix} Q_{ny} \\ Q_{sy} \\ Q_{sy} \end{bmatrix} \tag{11}$$

The softening constitutive law for the normal interface force is shown in Fig. 4. It represents a single-branch softening curve with λ_{nc} being the critical crack opening displacement. The vertical paths represent either elastic loading or unloading. Along the softening path, the multiplier can only have positive increasing values unless unloading occurs. After the critical opening displacement is exceeded, the crack opens or closes freely and the multiplier can increase or decrease in value.

A similar softening constitutive law for the shear force at the interface node is assumed with, namely, a single-branch softening curve with λ_{sc} being the critical shear displacement.

The evolution of the inelastic failure surface is represented by an interface hardening (softening) matrix $\mathbf{H_i}$. If the multipliers have not exceeded their critical values then the general form of the matrix $\mathbf{H_i}$ is defined by
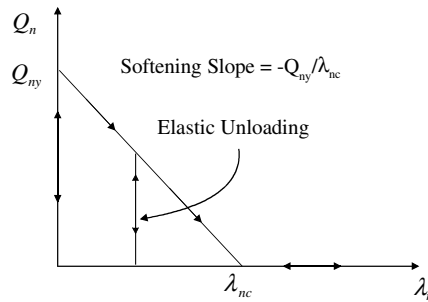
Fig. 4. Interface single branch softening constitutive law.

$$\mathbf{H_i} = \begin{bmatrix} -\dfrac{Q_{\mathrm{ny}}}{\lambda_{\mathrm{nc}}} & \dfrac{\beta Q_{\mathrm{ny}}}{\lambda_{\mathrm{sc}}} & \dfrac{\beta Q_{\mathrm{ny}}}{\lambda_{\mathrm{sc}}} \\[2mm] -\dfrac{\beta Q_{\mathrm{sy}}}{\lambda_{\mathrm{nc}}} & -\dfrac{Q_{\mathrm{sy}}}{\lambda_{\mathrm{sc}}} & 0 \\[2mm] -\dfrac{\beta Q_{\mathrm{sy}}}{\lambda_{\mathrm{nc}}} & 0 & -\dfrac{Q_{\mathrm{sy}}}{\lambda_{\mathrm{sc}}} \end{bmatrix} \tag{12}$$

The off-diagonal terms in the matrix above represent interaction between softening of the normal interface force and the interface shear capacity. The β term is a scaling factor for this interaction. A β value of unity ensures that the inelastic failure surface contracts in an isotropic manner. In mode I fracture, the β factor can also be used to prescribe a level of aggregate interlock. This will be discussed further in the examples. No interaction between the two interface shear inelastic failure planes has been assumed. That is, if a shear inelastic failure plane is activated, the shear inelastic failure plane associated with a reversed shear load is not affected.

The evolution of the interface inelastic failure surface is defined by the vector ξ_i

$$\xi_i = \mathbf{r_i} + \mathbf{H_i}\lambda_i \tag{13}$$

4. Structure relations

The following section closely follows the classical plasticity formulation of Maier [15] (see also Refs. [16–20]). Generalized stresses and strains, in the present context, refer to interface forces and displacements, respectively. The interface normality matrix $\mathbf{N_i}$, the interface dilatancy matrix $\mathbf{V_i}$ and the interface softening matrix $\mathbf{H_i}$ are assembled into block-diagonal matrices $\mathbf{N}$, $\mathbf{V}$ and $\mathbf{H}$, respectively. Note the following vectors and matrices are for the assembled structure.

The interface displacements are assumed to be the addition of recoverable elastic $\mathbf{q_e}$ and an inelastic $\mathbf{q_p}$ component. Therefore,

$$\mathbf{q} = \mathbf{q_e} + \mathbf{q_p} \tag{14}$$

The recoverable elastic interface displacements are further related to the interface forces through

$$\mathbf{Q} = \mathbf{S}\mathbf{q_e} \tag{15}$$

Fig. 5 shows diagrammatically the relationships defined in (14) and (15). From (1), (2) and (6), we can derive the following obvious expression for the recoverable elastic displacement components $\mathbf{u_e}$:
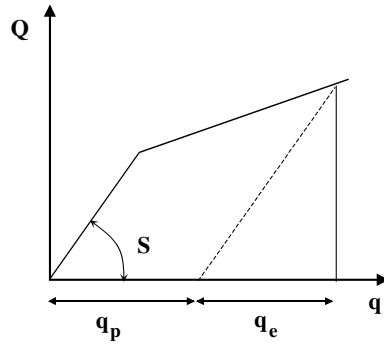
Fig. 5. Relationships between interface forces and displacements.

$$\mathbf{u_e} = \mathbf{K}^{-1}\alpha\mathbf{F} \tag{16}$$

where α is a scalar load factor.

The inelastic components of the interface displacements are given by

$$\mathbf{q_p} = \mathbf{N}\lambda \tag{17a}$$

for an associated flow rule and by

$$\mathbf{q_p} = \mathbf{V}\lambda \tag{17b}$$

for an nonassociated flow rule, where $\mathbf{N}$, $\mathbf{V}$ and λ are appropriately assembled quantities for the complete structure.

In the following derivations the nonassociated flow rule will be assumed (substituting $\mathbf{N}$ for $\mathbf{V}$ provides the associated case). Using (1), (2), (6) and (14)–(16), we obtain the total nodal displacements

$$\mathbf{u} = \mathbf{u_e} + \mathbf{K}^{-1}\mathbf{ASV}\lambda = \mathbf{u_e} + \mathbf{u_p} \tag{18}$$

where $\mathbf{u_p}$ is the inelastic component of the global displacements defined by

$$\mathbf{u_p} = \mathbf{K}^{-1}\mathbf{ASV}\lambda = \mathbf{R}\lambda \tag{19}$$

To determine the inelastic and elastic recoverable components of the interface forces, denoted by $\mathbf{Q_p}$ and $\mathbf{Q_e}$, respectively, we employ (2) and (14)–(18). Hence

$$\begin{aligned}
\mathbf{Q} &= \alpha\mathbf{Q_e} + \mathbf{Q_p} \\
\alpha\mathbf{Q_e} &= \mathbf{SA^TK}^{-1}\alpha\mathbf{F} \\
\mathbf{Q_p} &= (\mathbf{SA^TK}^{-1}\mathbf{ASV} - \mathbf{SV})\lambda = \mathbf{ZV}\lambda
\end{aligned} \tag{20}$$

Applying the equilibrium equation described in (1) on the level of the complete structure and employing (20), we find that

$$\mathbf{AQ_p} = \mathbf{AZV}\lambda = \mathbf{Ku_p} - \mathbf{ASq_p} = 0 \tag{21}$$

since $\mathbf{AZ} = \mathbf{0}$. The set of inelastic generalised interface forces $\mathbf{Q_p}$ define a set of forces in equilibrium with zero applied loads.

5. Nonholonomic rate formulation

Inelastic failure is activated if the interface generalised force vector $\mathbf{Q}$ reaches the inelastic failure surface (Fig. 6). The projections of $\mathbf{Q}$ in all phases must, therefore, satisfy the following condition:

$$\mathbf{N^T Q} \leqslant \mathbf{r} + \mathbf{H\lambda} = \boldsymbol{\xi} \tag{22}$$

where $\mathbf{r}$ is the vector of initial inelastic failure values, $\mathbf{H}$ is the hardening matrix and $\boldsymbol{\xi}$ is inelastic failure surface evolution vector. Using (20) and (22), we can write the following holonomic relations in total quantities:

$$\begin{aligned}
\boldsymbol{\varphi} &= \mathbf{N^T Q} - \mathbf{r} - \mathbf{H\lambda} \leqslant \mathbf{0} \\
&= \alpha \mathbf{N^T Q_e} - \mathbf{r} + (\mathbf{N^T ZV} - \mathbf{H})\lambda \leqslant \mathbf{0} \\
&= \alpha \mathbf{N^T Q_e} - \mathbf{r} + \mathbf{W\lambda} \leqslant \mathbf{0}
\end{aligned} \tag{23}$$

in which $\boldsymbol{\varphi}$ is a potential function vector. If the ith inelastic failure plane is active then the corresponding ith element of the potential vector $\boldsymbol{\varphi}$ is zero. The following constraints must also be satisfied:

$$\boldsymbol{\lambda} \geqslant \mathbf{0} \quad \boldsymbol{\varphi^T \lambda} = 0 \tag{24}$$

Initially, only positive or zero values for the multipliers are acceptable (this constraint will be relaxed for those multipliers which have exceeded the critical value). The multiplier vector $\boldsymbol{\lambda}$ and the function vector $\boldsymbol{\varphi}$ must be orthogonal. If the ith inelastic failure plane is active then $\varphi_i = 0$ while for the nonactive planes the corresponding multipliers must be zero. Complementarity must be satisfied at the holonomic level (i.e., in total quantities).

In order to capture critical events such as unloading and the start of a fully developed crack, a nonholonomic problem must be formulated and solved. This is can be cast in terms of "active" variables (active multipliers, etc.) in finite incremental form using (23) and (24). Active variables pertain to those points on either the descending branch (in the cohesive region or craze) or on the horizontal branch (Fig. 4); points on the unloaded branch are termed "inactive". The active set in fact needs to distinguish between these two types of points, since for a softening branch $\Delta\lambda$ is nonnegative, whereas it is free (i.e., can take negative values as well as is required by a crack opening or closing) on the horizontal branch.

In the following, the subscripts a and b, are used to refer to the active set of plastic multipliers on the descending branch and the active set on the horizontal branch, respectively. The generic finite step complementarity problem to be solved requires evaluation of quantities pertaining to both sets. In particular, the following LCP needs to be solved:
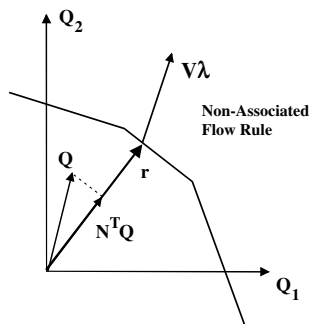

Fig. 6. Piece-wise linear failure surface.

$$\Delta\boldsymbol{\varphi}_a = \Delta\alpha\left\{ (\mathbf{N^T Q_e})_a - \mathbf{W}^*_{ab}(\mathbf{W}^*_{bb})^{-1}(\mathbf{N^T Q_e})_b + (\mathbf{W}^*_{aa} - \mathbf{W}^*_{ab}(\mathbf{W}^*_{bb})^{-1}\mathbf{W}^*_{ba})\frac{\Delta\boldsymbol{\lambda}_a}{\Delta\alpha} \right\}$$ (25)

$$\Delta\boldsymbol{\varphi}_a \leqslant \mathbf{0} \quad \Delta\boldsymbol{\lambda}_a \geqslant \mathbf{0} \quad (\Delta\boldsymbol{\varphi}_a)^{\mathbf{T}}\Delta\boldsymbol{\lambda}_a = 0$$

and $\Delta\boldsymbol{\lambda}_b$ then found from

$$\Delta\boldsymbol{\lambda}_b = -(\mathbf{W}^*_{bb})^{-1}\{(\mathbf{N^T Q_e})_b + \mathbf{W}^*_{ba}\Delta\boldsymbol{\lambda}_a\}$$ (26)

where the subscripting indicates an appropriate subset of the relevant quantity, Δ denotes a finite increment and the superscript *, such as for $\mathbf{W}^*_{aa}$, indicates the current value.

When $\{b\}$ is the null set, the LCP becomes

$$\Delta\boldsymbol{\varphi}_a = \Delta\alpha\left\{ (\mathbf{N^T Q_e})_a + \mathbf{W}^*_{aa}\frac{\Delta\boldsymbol{\lambda}_a}{\Delta\alpha} \right\}$$ (27)

$$\Delta\boldsymbol{\varphi}_a \leqslant \mathbf{0} \quad \Delta\boldsymbol{\lambda}_a \geqslant 0 \quad (\Delta\boldsymbol{\varphi}_a)^{\mathbf{T}}\Delta\boldsymbol{\lambda}_a = 0$$

The general LCP is commonly expressed as

$$\mathbf{z} = \mathbf{p} + \mathbf{Mx} \geqslant \mathbf{0} \quad \mathbf{x} \geqslant \mathbf{0} \quad \mathbf{z^T x} = 0$$ (28)

Unique solutions are guaranteed if the **M** matrix is positive definite and standard algorithms such that of Lemke [21] can be used to solve such instances. In the present case, when the **M** matrix is not symmetric, the symmetric part of the **M** matrix is checked for positive definiteness. When the **M** matrix is not positive definite a multiplicity of solutions can be possible indicating a bifurcation has been reached. An enumerative procedure to solve the LCP is used, as described in Bolzon et al. [7]. This approach has been adopted in the present work.

5.1. Quasiprescribed displacement control

Before we proceed to examine a suitable solution algorithm, the equations given in (23) will be recast in quasiprescribed displacement control which maintains proportional loading.

The displacement vector defined in (18) and (19) is rewritten as

$$\mathbf{u} = \alpha\mathbf{u}^*_e + \mathbf{R}\boldsymbol{\lambda}$$ (29)

where $\mathbf{u}^*_e$ is the elastic displacement vector for a unit load factor. Further, vector **u** can be split into a scalar term u_r (rth term of **u**) and a vector $\mathbf{u_s}$ such that

$$\mathbf{u} = \begin{bmatrix} u_r \\ \mathbf{u_s} \end{bmatrix} = \begin{bmatrix} \alpha u^*_{er} + \mathbf{R}_r\boldsymbol{\lambda} \\ \alpha\mathbf{u}^*_{es} + \mathbf{R}_s\boldsymbol{\lambda} \end{bmatrix}$$ (30)

In the above, u^*_{er} is the rth term of $\mathbf{u}^*_e$ and $\mathbf{R_r}$ is the rth row of **R**. Solving for the load factor, we have

$$\alpha = \frac{u_r}{u^*_{er}} - \frac{\mathbf{R}_r}{u^*_{er}}\boldsymbol{\lambda} = \eta - \mathbf{R}^*_r\boldsymbol{\lambda}$$ (31)

where η is the control displacement factor.

Substituting the above equation into (23) provides the finite incremental form for the potential function $\boldsymbol{\varphi}$, or

$$\Delta\boldsymbol{\varphi} = \Delta\eta\left\{ \mathbf{N^T Q_e} + (\mathbf{W}^* - \mathbf{N^T Q_e R}^*_r)\frac{\Delta\boldsymbol{\lambda}}{\Delta\eta} \right\}$$ (32)

The necessary modification can also be applied to (25) and (26). Other forms of control (e.g., stress, strain and external work) can be devised by noting that the load factor α can be written as a function of the multiplier vector in the general form

$$\alpha = \gamma + \mathbf{b}^{\mathbf{T}}\boldsymbol{\lambda} \tag{33}$$

with γ being a scaling factor and $\mathbf{b}$ a nonzero vector, and substituting into (23).

5.2. Solution algorithm

The problem is solved in incremental steps as a series of LCPs. Each step defines an single or multiple event in which the active set of multipliers is scaled either to the next inelastic point (or points if one allows simultaneous events) or until a multiplier (or multipliers) reaches a critical value. If one were to restrict the algorithm to only a single event at each step, this would reduce the number of possible multiple solutions. We call this a single event by event strategy. One could argue that nature would behave in this way, as one can see that if several locations within a structure simultaneously reach inelastic failure, the minimum work would be done if only one softens and the rest elastically unload (excluding the solution where all elastically unload).

From (24) and (32), the LCP is given by

$$
\begin{aligned}
\mathbf{z} &= \mathbf{p} + \mathbf{Mx} \quad \mathbf{x} \geqslant \mathbf{0} \quad \mathbf{z}^{\mathbf{T}}\mathbf{x} = 0 \\
\mathbf{z} &= -\Delta\boldsymbol{\varphi} \quad \mathbf{x} = \Delta\boldsymbol{\lambda} \quad \mathbf{z} \geqslant \mathbf{0} \\
\mathbf{p} &= -\Delta\eta\mathbf{N}^{\mathbf{T}}\mathbf{Q_e} \quad \mathbf{M} = (\mathbf{N}^{\mathbf{T}}\mathbf{Q_e}\mathbf{R}_r^* - \mathbf{W}^*)
\end{aligned} \tag{34}
$$

The steps in the solution algorithm are:

1. The initial inelastic failure set of multipliers is determined from

$$\eta_o = \min\left(\frac{\mathbf{r}(j)}{\mathbf{N}^{\mathbf{T}}\mathbf{Q}_e(j)} > 0\right) \quad \forall j \in \text{set of potentials} \tag{35}$$

   where η_o is the initial scaling factor. Eq. (35) is used to identify a set of initial active multipliers "x" and a nonactive set "y". The initial values for the potential function are then

$$\boldsymbol{\varphi}_o = \mathbf{r} - \eta_o\mathbf{N}^{\mathbf{T}}\mathbf{Q_e} \tag{36}$$

   and the initial values for the evolution of the inelastic failure surface vector are set equal to $\boldsymbol{\xi}_o = \mathbf{r}$. The first event is taken as the initial inelastic failure.
2. To reduce the storage space, the elements associated with the active set are only required in the formation of the $\mathbf{W}^*$ and $\mathbf{R}_r^*$ matrices. These matrices are assembled at each increment. The $\mathbf{p}_x$ and $\mathbf{M}_{xx}$ matrices are determined for the active set "x". The symmetric part of the $\mathbf{M}_{xx}$ matrix is then checked to see if it is positive definite. For the active set, (32) becomes

$$\Delta\boldsymbol{\varphi} = \Delta\eta\left\{\mathbf{p}_x + \mathbf{M}_{xx}\frac{\Delta\boldsymbol{\lambda}}{\Delta\eta}\right\} \tag{37}$$

   The increment in the control displacement factor $\Delta\eta$ is initially set to unity. If the $\mathbf{M}_{xx}$ matrix is positive definite, the Lemke routine [21] is used to solve the LCP for a unique solution. If no solutions exit, then the possibility of snapback is checked. This is done by solving the LCP with $\Delta\eta = -1$.
   When the $\mathbf{M}_{xx}$ matrix is not positive definite, an enumerative procedure can be employed to check for bifurcation of the equilibrium path and capture possible multiple solutions. This is done for both $\Delta\eta = +1$ and -1. When multiple solutions exist, a bifurcation has been encountered and the solution

which provides the minimum increment in external work is taken as the critical solution. This is seen as very important when investigating softening and especially so for interacting and/or branching cracks. To determine the increment in the external work, the load factor increment is first calculated from

$$\Delta\alpha = \Delta\eta - \mathbf{R}_r^*\Delta\lambda \tag{38}$$

The displacement increments conjugate to the load freedoms are then computed as well as the external increment in work. Total unloading of all multipliers (total elastic unloading) is excluded from the solution set. When all the solutions provide positive increments in the external work, the solution corresponding to the minimum increment is chosen. When solutions provide negative increments in external work, the critical solution corresponds to the maximum increment.

3. The load path is traced by determining events corresponding to either the activation of the inelastic failure surface or an interface inelastic failure surface contracting to zero (corresponding to unrestrained movement). Each event is linear in $\Delta\lambda$. The control displacement increment for the next inelastic failure event is hence calculated from

$$\Delta\eta_{\text{next yield}} = \min(\boldsymbol{\varphi}(j)/\Delta\boldsymbol{\varphi}(j)) \quad \forall j \in \text{nonactive set} \tag{39}$$

As well, the control displacement increment required for the next inelastic failure surface to contract to zero is determined from

$$\Delta\eta_{\text{critical}} = \min[\boldsymbol{\xi}(j)/\mathbf{H}^*(j,:)\Delta\lambda] \quad \forall j \in \text{active set on descending branch} \tag{40}$$

The critical displacement increment is determined from the minimum of (39) and (40). If this increment is associated with a fully contracted inelastic failure surface, the elements of the row and column of the hardening matrix associated with the contracted inelastic failure surface are set to zero. At each event, a set of active multipliers is maintained and updated, with points unloading removed from the active set. Unloading is detected when the increment to a multiplier is zero.

6. Inclined interfaces

If a mesh is randomly generated it is unlikely that the interfaces will be perpendicular to the principal tensile stress direction. Hence, interfaces closest to perpendicular to the principal tensile stress direction would be expected to reach inelastic failure first, but at a higher load to that if they were exactly perpendicular to the principal tensile stress direction. This problem is also compounded by the fact that the interface length L_i is longer than the perpendicular length L. Fig. 7a shows a material in pure tension with an inclined interface. The horizontal force applied is Q_i. The inclination of the interface to the vertical is defined by θ. From equilibrium, one can determine the relationship between the value of Q_i when the interface force reaches the inelastic failure surface, and the pure tensile strength given by $f_t L t_i$. Hence

$$Q_i = \frac{f_t L t_i}{[\cos(\theta)]^2} \tag{41}$$

To account for this misalignment, the interface tensile strength can be reduced by the factor

$$[\cos(\theta)]^2 \tag{42}$$

where θ is here referred to as the misalignment angle. As long as the inclination of the interfaces is less than the angle ϖ defined in Fig. 7b, inelastic failure will be tensile. For concretes, the angle ϖ is in the range of 70–80°. In the examples presented in this paper, if a misalignment angle is incorporated it is applied throughout the mesh.
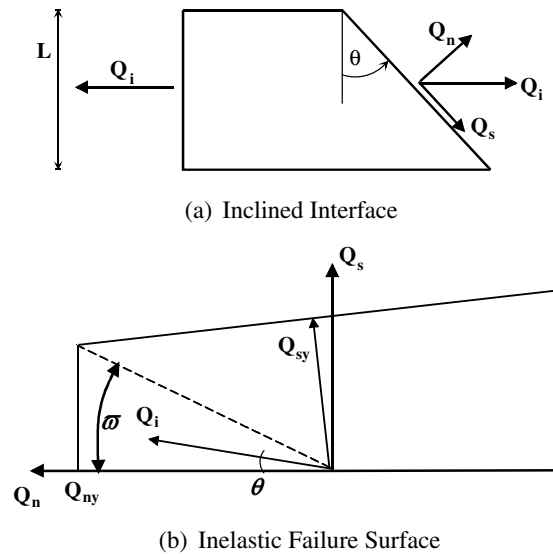
(a) Inclined Interface

(b) Inelastic Failure Surface

Fig. 7. Material with inclined interface subjected to pure tension.

7. Examples

7.1. Three point bending

The first example is that of an idealised three point bending test taken from Bolzon et al. [7]. The simply supported plain concrete beam (without a notch), is loaded by a concentrated load at mid-span. The length of the beam is 400 mm, while the width and depth are 100 mm. The elastic modulus of the concrete is taken as $E_c = 14,700$ MPa, Poisson's ratio $v = 0.1$, the tensile strength $\sigma_{ty} = 1.285$ MPa and the critical normal crack opening displacement $\lambda_{nc} = 0.03$ mm.

Two meshes were generated using a Delaunay triangulation algorithm. One had a prescribed straight boundary at mid-span (Mesh 1 in Fig. 8). Mesh 2 (Fig. 9) had no prescribed boundary. Using a mis-alignment angle of 20°, the tensile strength for Mesh 2 was set to 1.135 MPa.

The load versus load point deflection results obtained are shown in Figs. 10 and 11. The discrepancy between the initial slope of the simulations and the results of Bolzon et al. [17] is because the load point deflection is plotted and this is slightly different for the two meshes. Both meshes, however, show good agreement with the results of Bolzon et al. [7].

When the shear tension interaction factor β is set to zero (recall Eq. (12)) for Mesh 2, the softening response shown in Fig. 11 has a residual in its tail due to the shear that can be carried across the inclined interfaces. When the shear tension interaction factor β is set to unity no shear can be carried across the
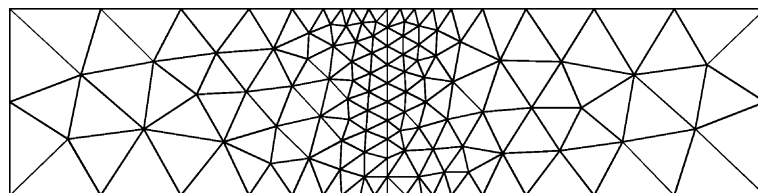
Fig. 8. Three point bending simulation—Mesh 1.
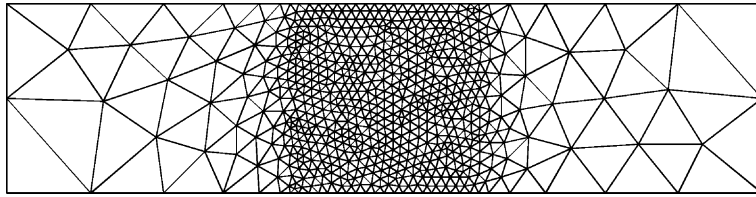
Fig. 9. Three point bending simulation—Mesh 2.
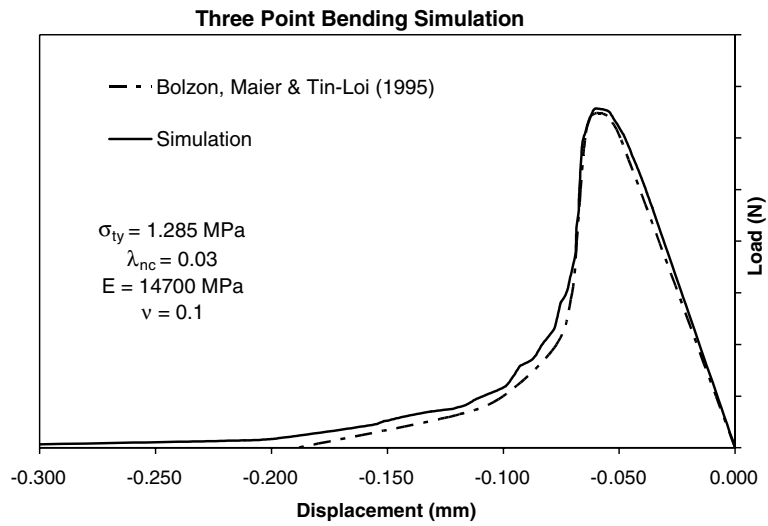
Fig. 10. Simulation of three point bending test—Mesh 1.
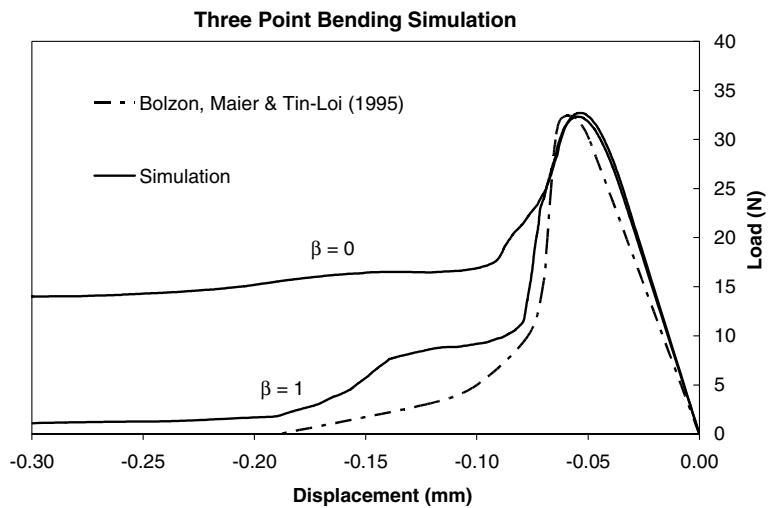
Fig. 11. Simulation of three point bending test—Mesh 2.

(a) β=0.

(b) β=1.
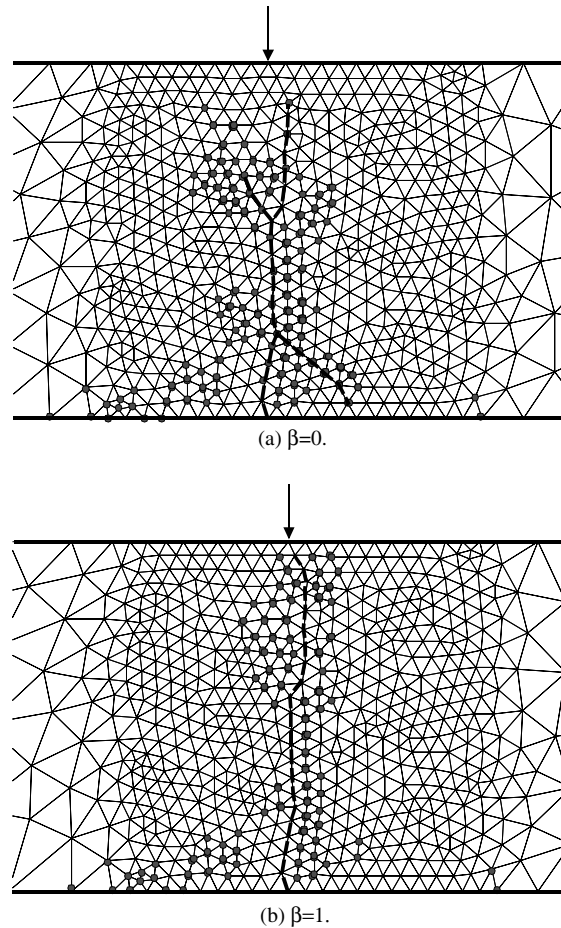
Fig. 12. Crack path—Mesh 2. ◉—Nonactive failure (elastically unloading/loading).

opening cracks and the softening response has no residual shear. Fig. 12a and b shows the crack path for Mesh 2 and the location of points which reached inelastic failure but elastically unloaded at some stage during the simulation. The damage zone is reflected by the nonactive failure points. The crack path is defined by those points that reached the critical crack opening displacement. For Mesh 2, the crack path traced approximates a straight path from the mid-span to the loading point. When the shear tension interaction factor β is zero, the opening cracks are restrained because shear can still be carried across them. As a consequence the generated crack path (see Fig. 12a) has two branching arms which do not appeal in the simulation with β equal to unity. There was only one solution to the LCP at all the events along the load versus deflection curve indicating that there was no branching of the equilibrium path. Fig. 13 shows the scaled deflected shape based on the total deflections at the nodal points for Mesh 2 ($\beta = 1$).

7.2. Two notched tensile—severe snap back problem

The second example is again taken from Bolzon et al. [3]. The two notched tensile problem has been studied extensively in the literature and is considered a benchmark test for formulations used in the analysis
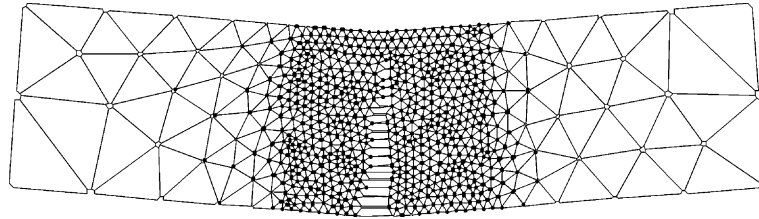
Fig. 13. Scaled deflected shape—Mesh 2 ($\beta = 1$).

of brittle fracture. Multiple solutions to the equilibrium path exist and are related to whether the end platens are allowed to rotate or are fixed.

The material parameters chosen in Bolzon et al. [3] were adopted to produce a severe snap-back response. The length of the tensile specimen was taken as 250 mm, the depth as 60 mm, the elastic modulus of the concrete $E_c = 18,000$ MPa, Poisson's ratio $v = 0.2$, tensile strength of the concrete $\sigma_{ty} = 3.4$ MPa and the critical crack opening displacement $w_c = 0.0105$ mm. Two notches 5 mm deep on each side at mid-span were included. A symmetric mesh was generated for this idealised problem with a straight vertical interface boundary at the mid-span of the specimen as shown in Fig. 14. An axial displacement at one of the load points was used as a control variable. Fig. 15a shows all solutions tracked by the solution algorithm. As the load increased two cracks initially formed at the two notches with both cracks propagating towards the centre. Fig. 15b provides a close-up of the bifurcation points near the peak load. There were several bifurcation points associated with allowing the loading platen to rotate and permitting one crack to propagate while the other closed. The stress deflection response with the largest stress carried was the solution where the platens remained fixed and the two cracks simultaneously propagated to the centre of the beam. Fig. 15c shows the results of the simulation using a single event by event strategy. It can be seen that the single event by event strategy produced the critical equilibrium path for the idealised problem associated with an asymmetric mode of failure.

Bolzon et al. [3] used a boundary element with the crack path prescribed. The advantage of the proposed formulation is that the crack path does not need to be known "a priori" and the formulation can be used for interacting and branching cracks.

7.3. Experimental SEN four point bending

The third example consists of a simulation of the SEN—single edge notched beam under four point bending test results of Schlangen [22]. The SEN experiment is a benchmark problem which has been studied extensively in the literature (see Geers et al. [23]). The SEN experimental setup was initially proposed to study mixed-mode fracture but was later shown to only involve mode I fracture. The details of the SEN test setup used by Schlangen [22] are shown in Fig. 16. The thickness of the specimen was 50 mm. The material
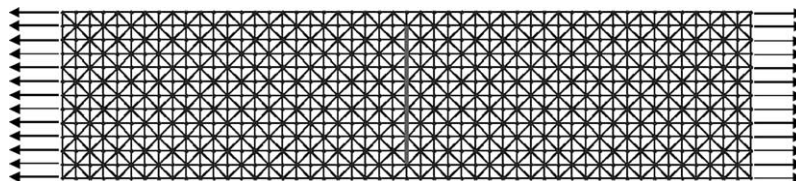

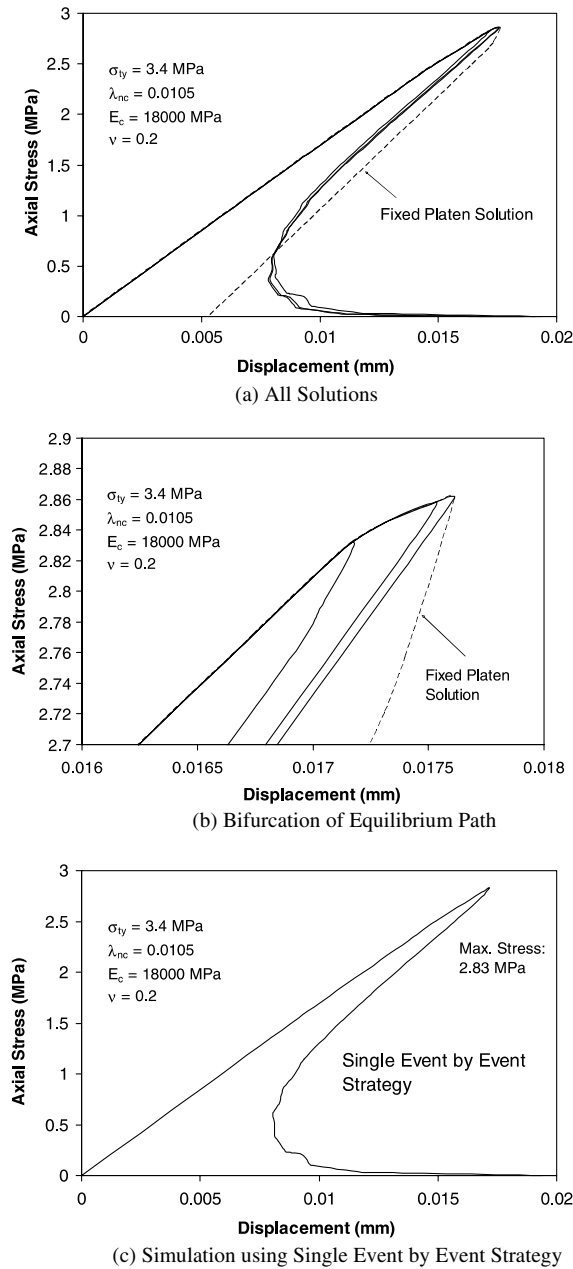Fig. 14. Mesh for the two notched tensile simulation.

(a) All Solutions

(b) Bifurcation of Equilibrium Path

(c) Simulation using Single Event by Event Strategy

Fig. 15. Simulation of the idealised two notched tensile test of Bolzon et al. [3].

properties assumed for the simulation were: $\sigma_{\text{ty}} = 3.0$ MPa, $E_{\text{c}} = 35,000$ MPa, $v = 0.2$, $\lambda_{\text{nc}} = 0.03$ mm, $\beta = 0.8$ and $\theta = 20°$. The deflection δ_1, is measured under the central load while δ_2 is the deflection measured under the end load.

Fig. 17 shows three meshes of increasing fineness generated using the Delaunay triangulation algorithm. The three meshes were used to study the mesh dependence of the formulation. Before the meshes are
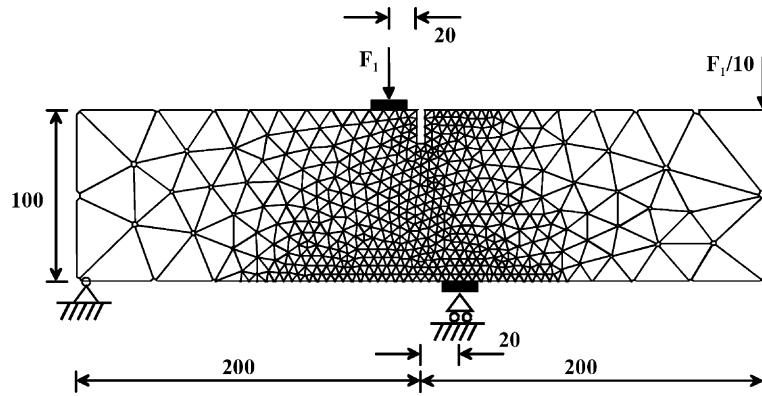
Fig. 16. SEN test setup.
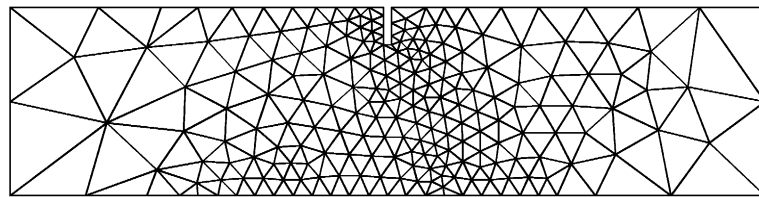
(a) Mesh 1
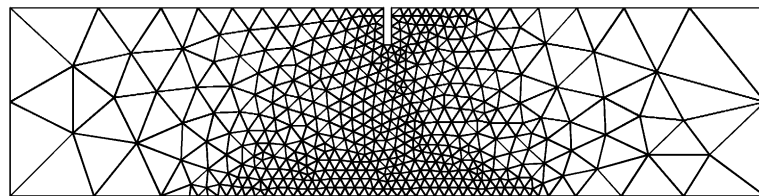
(b) Mesh 2
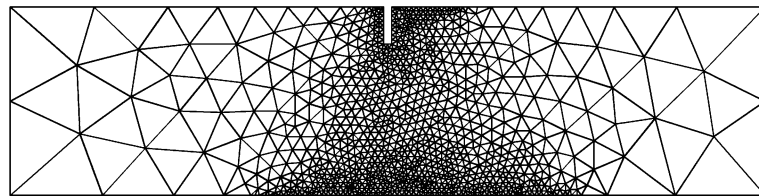
(c) Mesh 3

Fig. 17. Meshes used in the simulation.

compared, a simulation was conducted using the fineness mesh, Mesh 3 with values of β of 0, 0.8 and 1. As can be seen in Fig. 18, a β of 0.8 gives the best results for the tail of the post cracking response. The load versus the deflection δ_2 for the three meshes using a $\beta = 0.8$, are shown in Fig. 19. Qualitatively good agreement can be observed between the three meshes and the test results.
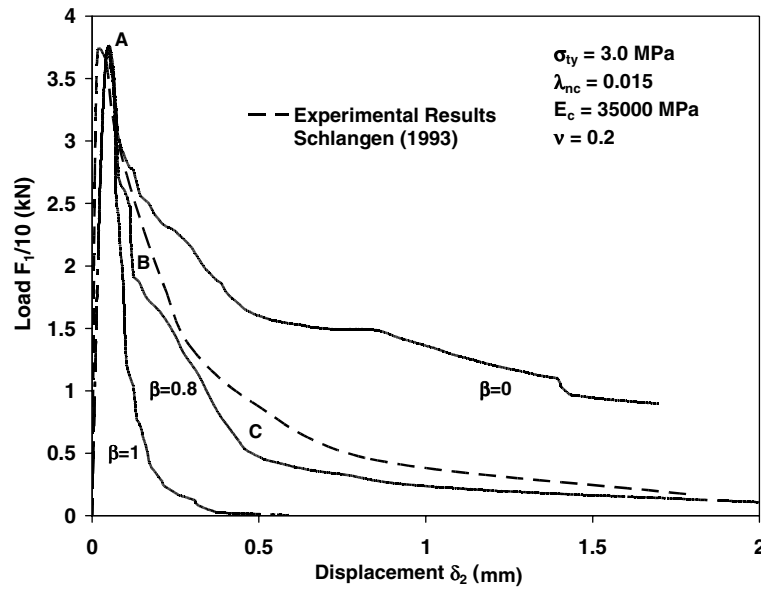
Fig. 18. Comparison of the effect of the tension–shear interaction factor β for Mesh 3.
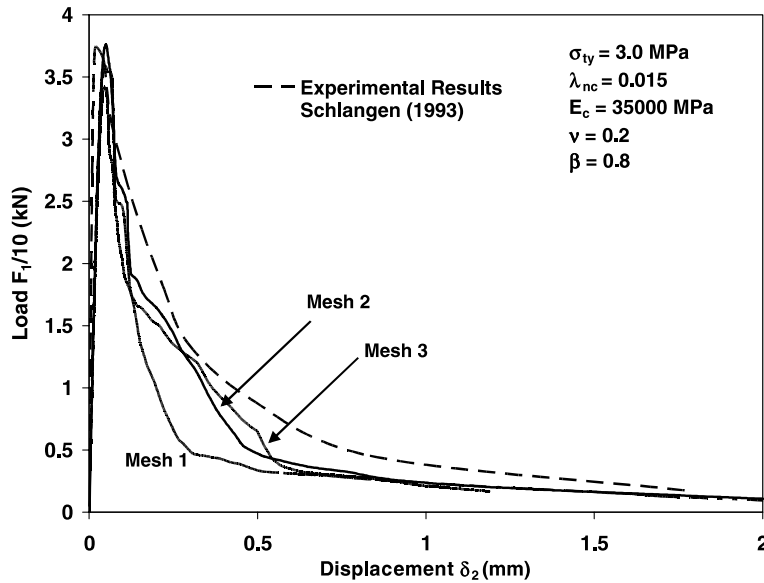
Fig. 19. Load versus deflection for SEN test for the three meshes studied.

A comparison of the load versus deflections δ_1 and δ_2, between the simulation and the test results for Mesh 3 are also shown in Fig. 20, again showing qualitatively good agreement. The observed crack path in the tests of Schlangen [22] is a curved crack starting at the notch and follows a curved path to the opposite support (see Fig. 25). Figs. 21–24 detail the inelastic failure zones at several stages along the softening path.
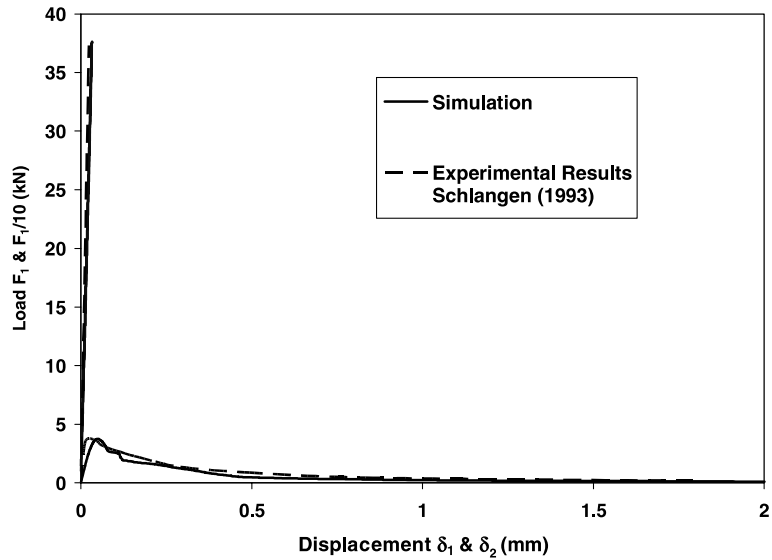
Fig. 20. Comparison of simulation with test results of Schlangen [22].
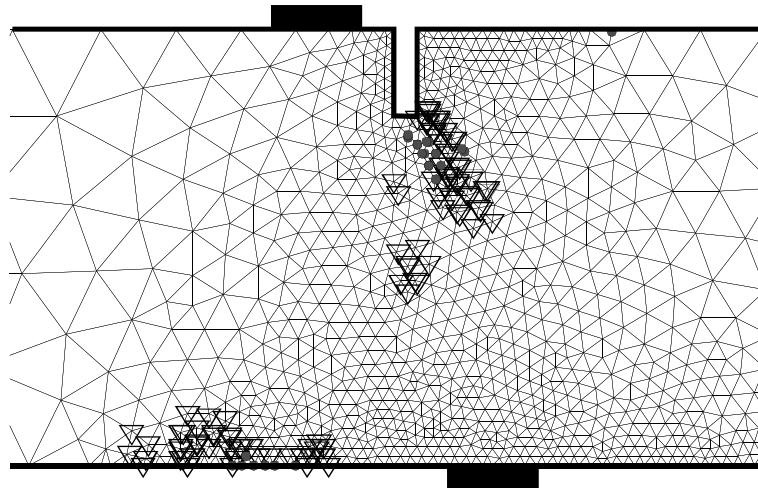
Fig. 21. Failure points at A. ▽—Tensile failure; △—shear failure; ○—critical displacement; ●—nonactive failure (elastically unloading/loading).

Fig. 26 shows the deflected shape at the end of the simulation run. The simulation results also show a curved crack path but indicate a branching crack from the notch. At the peak load, inelastic failure is only due to activation of the tension inelastic failure surface as can be seen in Fig. 21. This confirms that cracking is predominately of mode I type for this problem. At the peak load there are several inelastic failure zones, one near the notch and others near the opposite support. Figs. 22 and 23 show that as localization occurs during softening (when the critical opening displacement is reached near the notch), the inelastic failure points at the bottom of the beam elastically unload.
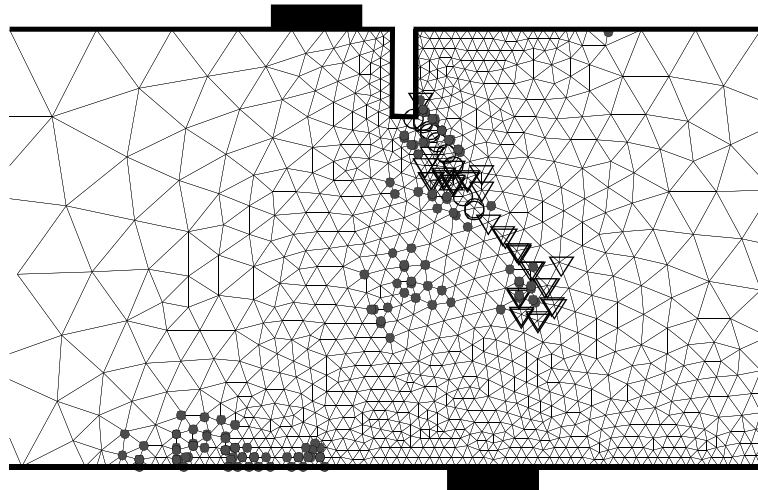
Fig. 22. Failure points at B. ▽—Tensile failure; △—shear failure; ○—critical displacement; ◉—nonactive failure (elastically unloading/loading).
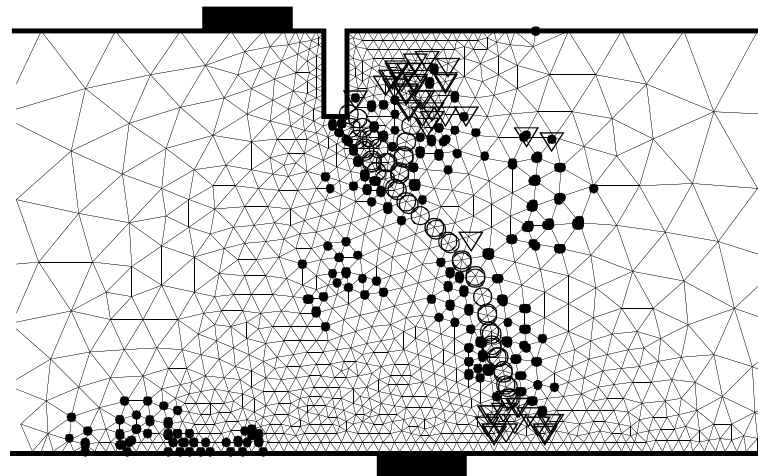

Fig. 23. Failure points at C. ▽—Tensile failure; △—shear failure; ○—critical displacement; ●—nonactive failure (elastically unloading/loading).

7.4. Gravity concrete dam

The Italian National Electric Board commissioned research in the early 1990s to assess the stability of existing unreinforced gravity concrete dams that crack under hygrothermal loads. As part of that research Carpinteri et al. [24] tested a prototype dam model with a preexisting notch on the upstream face of the dam. Point loads were applied on the upstream face to simulate the equivalent force from a water column. The loading induced a curved crack that propagated from the tip of the preexisting notch towards the downstream face of the dam. The experimental details are contained in Carpinteri et al. [24], Barpi and
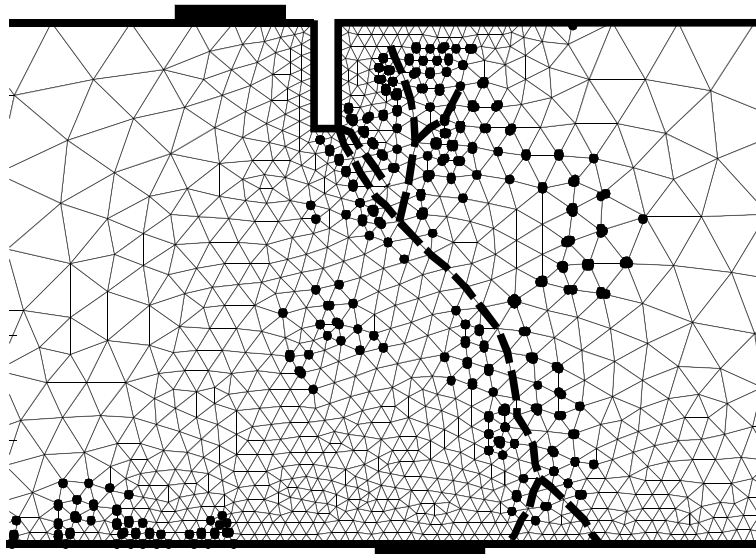
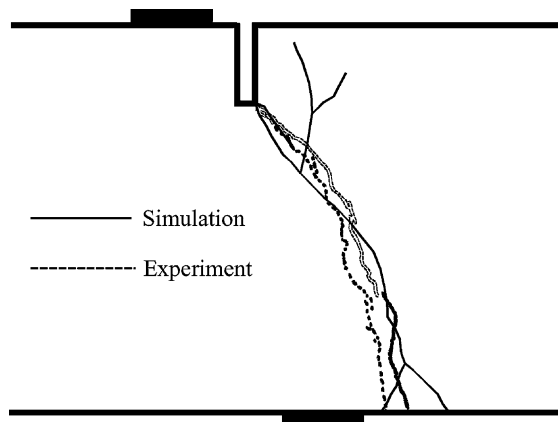Fig. 24. Crack path—Mesh 3. ●—Nonactive failure (elastically unloading/loading).

Fig. 25. Comparison of simulation crack path with test results of Schlangen [22].

Valente [25] and Oliver et al. [26]. A simulation was carried out using the proposed formulation to demonstrate an application to an important problem. The material properties assumed for the simulation were: $\sigma_{\text{ty}} = 3.6$ MPa, $E_c = 35,700$ MPa, $v = 0.1, \lambda_{\text{nc}} = 0.08$ mm, $\beta = 0.9$ and $\theta = 20°$. The mesh details and a comparison of the crack path with the experimental results are shown in Fig. 27. In Fig. 28, the load versus CMOD from the simulation is compared to the test result. Both the load versus CMOD and the crack trajectory show very good agreement between the simulation and the test results. Inelastic failure during the simulation was only activated by the tension inelastic failure surface indicating that fracture was predominately of mode I. Fig. 29 shows the scaled deflected shape at the end of the loading cycle.
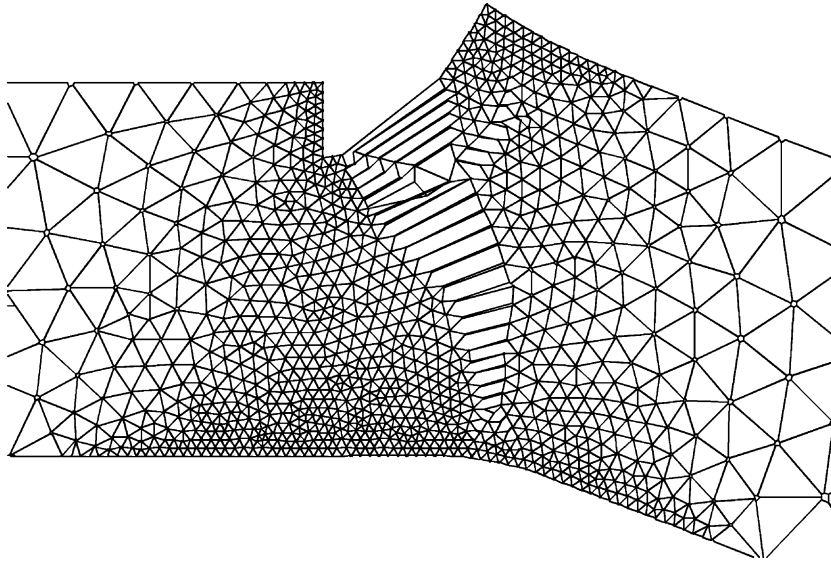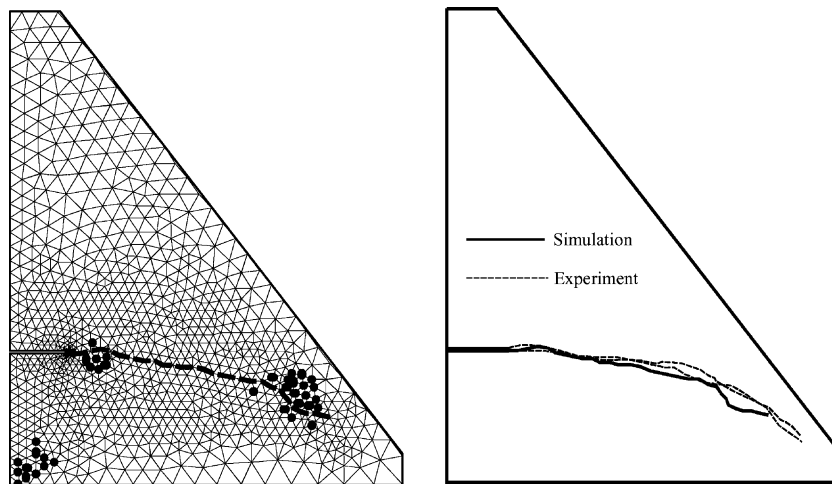
Fig. 26. Scaled deflected shape.

Fig. 27. Results of simulation for crack path.

8. Conclusions

A discrete triangular unit, constructed from constant strain triangles with nodes along its sides has been developed for the simulation of quasibrittle fracture. Fracture is captured through a constitutive softening–fracture law at the interface nodes. A linear softening law with a single softening branch was adopted. Since the softening law is formulated in terms of the forces and displacements at the interface nodes, no internal length scale or higher-order continuum structure was required. The path-dependent softening behaviour was solved in nonholonomic rate form. At each event in the loading history, solutions to an appropriate complementarity problem were obtained. When multiple solutions were detected, the equilibrium solution
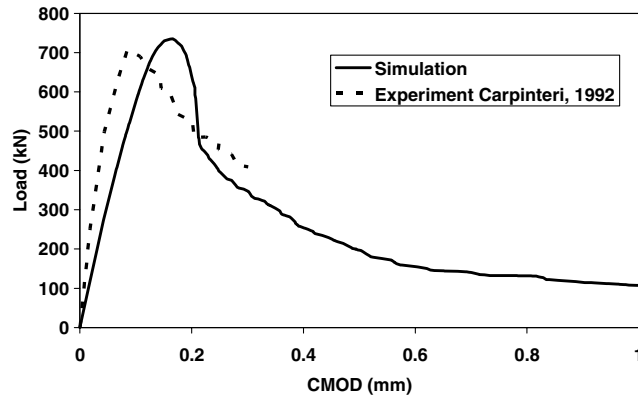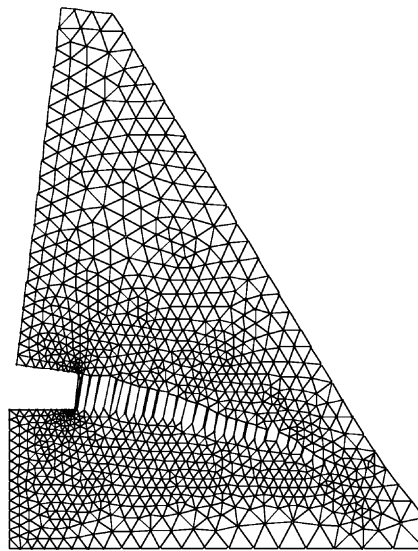
Fig. 28. Comparison of load versus CMOD.

Fig. 29. Scaled deflected shape, showing crack opening.

with the minimum increment in external work was adopted. Several examples involving mode I fracture were presented and compared to known solutions. Good results were obtained in addition to the robustness of the procedure in capturing the severe snap-back solution of the two notched tensile problem examined by Bolzon [3]. Current work is aimed at applying the same methodology to the solution of problems with unknown, possibly interacting crack itineraries and incorporating the heterogeneous nature of concrete by modelling aggregates, mortar and the aggregate–mortar bond regions separately.

References

[1] Li X, Cescotto S. Finite element method for gradient plasticity at large strains. Int J Numer Methods Engng 1996;39:619–33.
[2] De Borst R. Fracture in quasi-brittle materials: a review of continuum damage-based approaches. Engng Fract Mech 2002;69:95–112.

[3] Bolzon G, Maier G, Tin-Loi F. On multiplicity of solutions in quasi-brittle fracture computations. Comput Mech 1997;19:511–6.
[4] Hillerborg A, Modéer M, Petersson PE. Analysis of crack formation and crack growth in concrete by means of fracture mechanics and finite elements. Cem Concr Res 1976;6(6):773–82.
[5] Elices M, Guinea GV, Gómez J, Planas J. The cohesive zone model: advantages, limitations and challenges. Engng Fract Mech 2002;69:137–63.
[6] Bazant ZP. Concrete fracture models: testing and practice. Engng Fract Mech 2002;69:165–205.
[7] Bolzon G, Maier G, Tin-Loi F. Holonomic and nonholonomic simulations of quasi-brittle fracture: a comparative study of mathematical programming approaches. Fracture mechanics of concrete structures. In: Folker H, editor. Proceedings FRAMCOS 2. Freiburg: Wittmann; 1995. p. 885–98.
[8] Carol I, Prat PC, Lopez CM. Normal/shear cracking model: application to discrete crack analysis. J Engng Mech 1997;123(8):765–73.
[9] Van Mier JGM, Schlangen E, Vervuurt A, Van Vliet, MRA. Damage analysis of brittle disordered materials: concrete and rock. Mechanical behaviour of materials. In: Bakker A, editor. Seventh International Conference on Mechanical Behaviour of Materials—ICM7. Delft, The Netherlands: Delft University Press; 1995. p. 101–26.
[10] Schlangen E. Computational aspects of fracture simulations with lattice models. Fracture mechanics of concrete structures. In: Folker H, editor. Proceedings FRAMCOS-2. Freiburg: Wittmann; 1995. p. 913–28.
[11] Zubelewicz A, Bazant ZP. Interface element modelling of fracture in aggregate composites. ASCE J Engng Mech 1987;113(11):1619–30.
[12] Bazant ZP, Tabbara MR, Kazemi MT, Pijaudier-Cabot G. Random particle model for fracture of aggregate or fibre composites. ASCE J Engng Mech 1990;116(8):1686–705.
[13] Beranek WJ, Hobbelman GJ. 2D and 3D-modelling of concrete as an assemblage of spheres, revaluation of the failure criterion. Fracture mechanics of concrete structures. In: Folker H, editor. Proceedings FRAMCOS-2. Freiburg: Wittmann; 1995. p. 965–78.
[14] Attard MM, Tin-Loi F. Fracture simulation using a discrete triangular element. In: Bradford MA, Bridge RQ, Foster SJ, editors. ACMSM 16. Sydney, NSW, Australia: A.A. Balkema; 1999. p. 11–6.
[15] Maier G. A matrix structural theory of piecewise-linear elastoplasticity with interacting yield planes. Meccanica 1970;5:54–66.
[16] Maier G. Incremental plastic analysis in the presence of large displacements and physical instabilizing effects. Int J Solids Struct 1971;7:345–72.
[17] De Donate O, Maier G. Mathematical programming methods for the inelastic analysis of reinforced concrete frames allowing for limited rotation capacity. Int J Numer Methods Engng 1972;4:307–29.
[18] Wakefield RR, Tin-Loi F. Large scale nonholonomic elastoplastic analysis using a linear complementarity formulation. Comput Methods Appl Mech Engng 1990;84:229–42.
[19] Tin-Loi F, Misa JS. Large displacement elastoplastic analysis of semirigid steel frames. Int J Numer Methods Engng 1996;39:741–62.
[20] Cocchetti C, Maier G. Elastic–plastic and limit-state analyses of frames with softening plastic-hinge models by mathematical programming. Int J Solids Struct 2003;40:7219–44.
[21] Lemke CE. Bimatrix equilibrium points and mathematical programming. Manage Sci 1965;11:681–9.
[22] Schlangen E. Experimental and numerical analysis of fracture processes in concrete. Heron, Technical University of Delft, Delft, The Netherlands: 1993;38(2).
[23] Geers MGD, de Borst R, Peerlings RHJ. Damage and crack modeling in single-edge and double-edge notched concrete beams. Engng Fract Mech 2000;65:247–61.
[24] Carpinteri A, Valente S, Ferrara G, Imperato L. Experimental and numerical fracture modelling of a gravity dam. In: Bazant ZP, editor. Fracture mechanics of concrete structures. Amsterdam, The Netherlands: Elsevier Science; 1992. p. 351–60.
[25] Barpi F, Valente S. Numerical simulation of prenotched gravity dam models. J Engng Mech ASCE 2000;126(6):611–9.
[26] Oliver J, Huespe AE, Pulido MDG, Chaves E. From continuum mechanics to fracture mechanics: the strong discontinuity approach. Engng Fract Mech 2002;69:113–36.